

Three-Dimensional Molecular Mapping of Ionic Liquids at Electrified Interfaces

Shan Zhou^{1,2†}, Kaustubh S. Panse^{1,2†}, Mohammad Hossein Motevaselian^{3†}, Narayana R. Aluru^{3*} and Yingjie Zhang^{1,2*}

1. Department of Materials Science and Engineering, University of Illinois, Urbana, IL 61801, USA

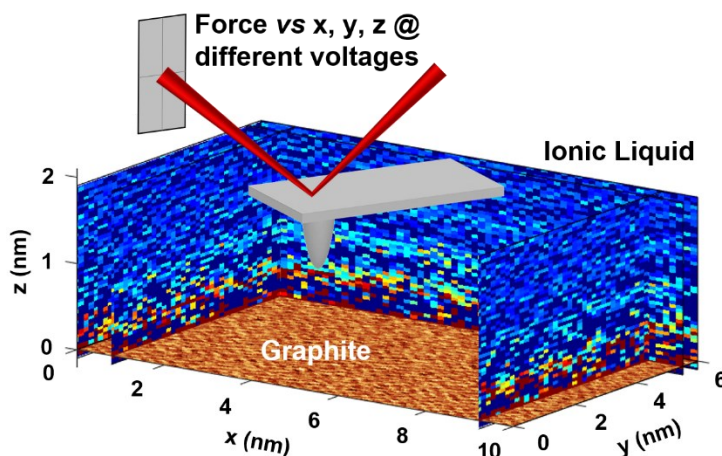
2. Materials Research Laboratory, University of Illinois, Urbana, IL 61801, USA

3. Department of Mechanical Science and Engineering, University of Illinois, Urbana, IL 61801, USA

†These authors contributed equally to this work

*Correspondence to: yjz@illinois.edu (Y.Z.) or aluru@illinois.edu (N.R.A.)

ToC figure:



ABSTRACT: Electric double layers (EDLs), occurring ubiquitously at solid-liquid interfaces, are critical for electrochemical energy conversion and storage processes such as capacitive charging and redox reactions. However, to date the molecular scale structure of EDLs remains elusive. Here we report an advanced technique, electrochemical three-dimensional atomic force microscopy (EC-3D-AFM), and use it to directly image the molecular scale EDL structure of an ionic liquid under different electrode potential. We observe not only multiple discrete ionic layers in the EDL on a graphite electrode, but also quasi-periodic molecular density distribution within each layer. Furthermore, we find pronounced 3D reconfiguration of the EDL at different voltage, especially in the first layer. Combining the experimental results with molecular dynamics (MD) simulations, we find potential-dependent molecular redistribution and reorientation in the innermost EDL layer, both of which are critical to EDL capacitive charging. We expect this mechanistic understanding to have profound impacts on the rational design of electrode-electrolyte interfaces for energy conversion and storage.

KEYWORDS: electrochemical AFM, 3D-AFM, ionic liquid, electric double layer, solid-liquid interface, electrode-electrolyte interface.

Solid-liquid interfaces are critical for a large range of natural and engineered systems ranging from electrochemical energy conversion and storage (*e.g.* batteries, supercapacitors, and fuel cells)^{1–4} to water filtration,^{5,6} corrosion control⁷ and cell biology.^{8–10} Due to the molecular interaction with the solid surface and the presence of local electric fields, liquid ions/molecules tend to reorganize to form discrete layer(s) near solid surfaces. These solvation layers, also called the EDLs, are key to realizing the desired functionalities at solid-liquid interfaces. For example, in supercapacitors, molecular arrangement in EDL directly determines the capacitive charge storage capabilities;^{11,12} in batteries, EDL structure modulates the kinetic barrier for Li⁺ ion intercalation and the growth of solid electrolyte interphase (SEI) layers, both of which have strong impacts on the energy density and stability.^{4,13–18} However, to date the molecular scale structure of EDL remains largely unknown. Most of the existing atomistic imaging and spectroscopy methods, such as electron and scanning tunneling microscopy and X-ray/optical spectroscopy, can only probe the binding states and/or planar distribution of strongly adsorbed species on the electrode surface, missing the 3D structure of the EDLs.^{19–21}

Based on sensitive force detection, AFM has been used to measure the EDL structures. By performing force-distance curves in the z direction (perpendicular to the solid surface) in various electrolytes, individual layers of EDL have been identified from discrete force spike features.^{18,22–31} However, these one-dimensional force curves do not provide information on the 3D molecular distribution. Recently, liquid phase 3D-AFM has been developed by a few labs, and was used to image EDLs.^{32–39} Operated in AC mode, and using either amplitude or frequency modulation, the tip-sample interaction force was mapped out in x, y (in-plane), and z (out-of-plane) directions, producing 3D images of the EDL structure. With a force sensitivity down to ~10 pN or lower, this technique was able to resolve both the atomic structure of the

solid surfaces and the molecular arrangement in EDLs. Despite these achievements, so far there has been no electrochemical potential control during the 3D-AFM imaging, preventing the understanding of structure-property relationship for charge and energy storage. In addition, existing 3D-AFM studies have been limited to aqueous electrolytes. The various organic electrolytes used in batteries and supercapacitors are highly viscous, resulting in significant damping of the tip oscillation, preventing high-resolution imaging using the existing AC mode 3D-AFM techniques.⁴⁰⁻⁴²

Building upon our previous success on high-speed 3D force mapping,⁴³ we have developed an EC-3D-AFM technique, by combining 3D-AFM with a sealed electrochemical cell for *in situ* imaging under controlled electrode potential and gas environment. We choose an ionic liquid (IL), 1-ethyl-3-methylimidazolium bis(trifluoromethylsulfonyl)imide (EMIM-TFSI), as the electrolyte, which has a large electrochemical window and low volatility, promising as a next generation electrolyte for energy storage.⁴⁴⁻⁴⁶ Previous AFM studies of ILs have been limited to 1D force-distance curve measurements, which have revealed multiple discrete layers with strong tip-molecule interaction (force typically reaching ~10 nN or more in the innermost layer).^{18,22-26,29-31} While another recent work measured 3D-AFM of an IL dissolved in water,⁴⁷ the obtained EDL structure is distinct from that of pure ILs, as evident from the much smaller force (~100 pN at the first layer) of the IL-in-water compared to that of pure ILs. Therefore, the 3D EDL structure of ILs on any solid surface remains unknown, even in simple conditions with no electrochemical potential control.

To overcome the limitations of existing 3D-AFM methods in measuring highly viscous liquids, we use DC mode and measure the tip-sample force *via* deflection detection, which overcomes the oscillation damping problem that occurs in AC mode. Through careful noise isolation, and by

choosing a relatively stiff cantilever, we are able to achieve 3D molecular resolution in a pure IL at controlled electrode potentials.

RESULTS AND DISCUSSION

EC-3D-AFM Setup and CV Measurements. A schematic of the setup is shown in Figure 1a, where the cantilever is immersed in a sealed, three-electrode electrochemical cell. The working electrode is a freshly cleaved highly oriented pyrolytic graphite (HOPG), while the counter and quasi-reference electrodes are both platinum. This EC cell is purged using argon before being sealed for EC-3D-AFM measurements. To enable 3D imaging, the tip is raster scanned on top of the electrode surface, with linear scan in the x-y direction and a simultaneous sinusoidal motion in the z direction (Figure 1b). The sinusoidal z motion has been shown to have low piezo noise at high z rate (*i.e.* larger than 10 Hz).^{35,48} The cantilever deflection is recorded as a function of x, y, and scanner extension (along the z direction) values. These data are further processed to obtain 3D maps that represent the real-space molecular density distribution.

Using this EC cell, we first measure the cyclic voltammetry (CV) of the EMIM-TFSI electrolyte (Figure 1c). We observe pronounced increase in current as the potential approaches ± 2 V, likely due to the intercalation of cations and anions as reported before.^{19,49,50} CV sweep over a smaller potential range of ± 1.5 V, as shown in Figure 1c inset, further reveals that EDL charging is the dominant process for the potential between -1 V and 1 V. Therefore, for EC-3D-AFM imaging, we restrict the potential to within ± 1 V throughout the whole measurement process. From the CV measurements in the range of ± 1 V (Supporting Information, Figure S1), we extract an accumulated capacitive charge per unit area of ~ 77 $\mu\text{C cm}^{-2}$ over a full potential cycle, which

corresponds to \sim 4.8 charges per nm². This indicates an average change of \sim 2.4 charges per nm² as the potential is swept from -1 V to 1 V. Considering that each ion in the IL carries only one charge, either positive or negative, such a large change in the density of capacitive charges implies a significant reconfiguration of the EDL.

EC-3D-AFM Imaging. We use electrically insulating tips for AFM imaging (see Methods), to ensure negligible electrostatic perturbations. Considering that the EDL structure is extremely sensitive to the surface chemistry and cleanliness of the electrode, it is important to determine the surface structure of HOPG before imaging the EDL. We find that most of the HOPG surface areas remain atomically clean within the chosen potential range of \pm 1 V. While small amounts of molecular cluster features are occasionally observed (Supporting Information, Figure S2), likely due to parasitic redox processes of trace amounts of impurities,^{51–53} these areas are avoided during 3D-AFM imaging.

To observe atomic and molecular scale features, we first perform AFM measurements at an electrode potential of 0 V vs Pt, which we find to be very close (within \sim 50 mV) to the open circuit potential (OCP). It is known that atomic resolution is difficult to achieve using height or deflection measurements in DC mode AFM, due to the finite radius of the tip-sample contact area.^{54–56} However, for clean crystalline materials, the lateral deflection signal in DC-AFM can accurately represent the crystalline lattice. We thus measure the lateral signal of the HOPG surface, and observe a hexagonal pattern with a lattice constant of \sim 0.25 nm (Figure 2a and Figure S3), consistent with the expected structure of HOPG. Therefore, we conclude that the imaged area of HOPG surface is atomically clean with no observable contamination. Note that previous reports on the force curve measurements of ILs did not show any lattice-resolution images of the substrate surfaces.^{18,22–31} The possible variations of the substrate cleanliness may

be one reason for the significant differences in the observed inter-layer spacing in the first 1-2 EDL layers.^{18,22-31}

We then measure a series of DC mode force curves on a clean spot of HOPG, to reveal the EDL structure along the z direction. The results of a total of 50 curves are shown in Figure 2b. For each force curve, the tip first approaches and reaches the HOPG surface, and then retracts away. During the approach, when the tip reaches each EDL layer, it is repelled by the ions inside the layer and thus retains its position as the force increases; when the force reaches a threshold, the tip ruptures the molecular layer, followed by a drop or flattening of force as the tip further moves downwards. Therefore, the point count at a given tip-sample distance (within a small interval) roughly represents the tip retention time and the molecular density at that position.

We further perform 3D-AFM measurements, and generate a point count at each x, y, and z value, and plot this 3D count histogram in Figure 2a. Detailed data processing procedures are provided in Supporting Information, Section 3. Besides revealing the clear layered structures which are consistent with the force curves in Figure 2b, the 3D map shows pronounced molecular density variations within each layer, in the form of quasi-periodic, zigzag-like patterns. Furthermore, by analyzing a series of x-z cross section maps, we find a consistent quasi-periodicity of 1.5 – 2 nm for all the observed layers. This size scale corresponds to roughly two times the length of individual EMIM⁺ or TFSI⁻ molecules,^{57,58} indicating that each zigzag feature may contain at least two ions in average.

To reveal the potential dependence of the EDL structure, we perform EC-3D-AFM imaging at other electrode voltages, including ± 0.5 V and ± 1 V. The full 3D count maps at all the five different voltages are shown as movies in the Supporting Information online (same color scale as

that in Figure 2a). Since most of the 3D molecular features are clearly represented in the x-z cross section images, we extract the x-z maps at different potentials, as shown in Figure 3a. We observe pronounced structural reconfigurations, especially at the first ionic layer. When the potential changes from 0 to ± 0.5 V, the 1st layer becomes wider and shows more pronounced zigzag oscillations; at ± 1 V, the 1st layer splits into two layers, with the lower layer being very close to the HOPG surface (~ 2 Å separation), and the upper layer ~ 5 Å above the lower one. In addition to the 1st layer, the 2nd and 3rd layers also show quasi-periodic zigzag oscillations, although the structure and separations of these upper layers do not exhibit clear potential-dependence. By summing the point counts over all the x values at each z point, we obtain the count histograms along the z axis (Figure 3b). These 1D histograms verify the multi-layer nature of the EDL structure and quantify the potential-dependent layer width and inter-layer distance, again revealing the widening and splitting behaviors of the 1st layer. These obtained layer positions also agree with those directly extracted from force-distance curves as shown in Figure 2b, which further confirms the validity of the point count method we use to produce 3D molecular density images.

To further verify the observed EDL structure, we perform EC-3D-AFM measurements of the same system, EMIM-TFSI on HOPG, using AC mode. Due to the strong oscillation damping effects in the viscous ILs, many of the AFM probes typically used for liquid phase AC mode imaging do not show clear oscillation peaks. Nevertheless, we are able to observe the first eigenmode using PPP-NCHAuD probes (Nanosensors) in EMIM-TFSI (Figure S5). Although the oscillation is strongly damped compared to that in air, it is sufficient to produce 3D-AFM images using the amplitude-modulation method. The obtained x-z images at five different electrode potentials (0, ± 0.5 V and ± 1 V) are shown in Figure S6, together with the

corresponding DC mode images (reproduced from Figure 3a). From the direct comparison of the AC and DC mode results at the series of different potentials, we can see that these two techniques produce very similar EDL structures, except that the resolution of the AC results are weaker – the zigzag features are not very clear and some upper layers cannot be resolved. These AC mode results both strongly prove the validity of our observed EDL structures, and reveal that the DC mode is better than AC mode in imaging highly viscous liquids.

The observed quasi-periodic zigzag features of EDL are likely due to the molecular tilt and/or the co-existence of cations and anions in each layer. When the potential is positive, the positively charged HOPG can pull the TFSI^- towards the surface and repel the EMIM^+ ; at negative potential, EMIM^+ may move towards the surface while TFSI^- will likely be repelled away. If the first layer initially consists of both EMIM^+ and TFSI^- at 0 V, then a non-zero potential can induce a vertical separation of the cations and anions, broadening the layer width, and eventually making the layer split. This may explain the potential-induced layer widening and splitting effects shown in Figure 3a, b. As to the molecular orientations, we expect the anions/cations in the 1st layer to be strongly attracted to the HOPG surface at highly positive/negative potentials, and become planar due to steric hindrance; at smaller potential or at upper layers, in addition to the interfacial electric field, the entropic effects, molecule-HOPG van der Waals (vdW) interaction, and inter-molecular Coulomb/vdW interaction should all contribute to the EDL structure, which may result in more random or tilted molecular orientations. These tentative explanations are consistent with the fact that the zigzag features in the 1st layer are more pronounced when they are farther away from the HOPG surface.

MD Simulations. To test and verify the above explanations of the experimentally observed EDL structure, we perform MD simulations of EMIM-TFSI ions sandwiched between two graphite

electrodes. The overall configuration of the simulated system is shown in Figure S7. Each graphite electrode consists of four layers of graphene sheets with a surface area of $7.122 \times 7.232 \text{ nm}^2$ and an inter-layer distance of 0.335 nm. The distance between the inner surfaces of the graphite electrodes is 16 nm, which ensures that the EDL at the two electrode-electrolyte interfaces do not interact.⁵⁹ In order to model the effect of an electric bias, we apply charges that uniformly distribute among the carbon atoms on the electrode surface, and the two opposite electrodes have the same absolute charge density with reverse sign. The electrode potential is obtained by integrating the charge density in the electrolyte using the Poisson's equation after the system equilibrates. We simulated systems with five different electrode surface charge density, 0, $\pm 0.28 \text{ e/nm}^2$, and $\pm 0.55 \text{ e/nm}^2$, where e is the elementary charge. Details of the calculated charge and potential distribution profiles in the EDL are shown in Figure S8. By comparing the differences in the obtained potentials at the electrode surfaces, we find that the five different electrode surface charge densities correspond to the potential of zero charge (PZC), $\text{PZC} + 0.93 \text{ V}$, $\text{PZC} - 0.90 \text{ V}$, $\text{PZC} + 1.97 \text{ V}$, and $\text{PZC} - 1.90 \text{ V}$, respectively. These parameters are in the same scale as the experimental conditions of 0, $\pm 0.5 \text{ V}$ and $\pm 1 \text{ V}$, and the charge density of $\sim 1.2 \text{ e/nm}^2$ upon 1 V charging (estimated from CV measurements). The small differences in capacitance are likely due to the leakage/parasitic currents in the CV measurements and/or the slight deviation of the MD force models from the realistic conditions. Despite the slightly lower overall charge density and higher potential in MD simulations, we find consistent trends of the potential-dependent EDL structural evolution in comparison with experimental results, as explained in the following paragraphs.

The simulated time-averaged atomic density profiles in the x-z plane are shown in Figure 4a. Similar to the experimental x-z maps, we observe discrete layered structures and quasi-periodic

variations in the atomic/molecular density. We also find pronounced reorganization of the first layer upon the change of potential, while upper layers show weaker potential dependence. We further extract the average molecular density of both EMIM^+ and TFSI^- as a function of z at different potentials, as shown in Figure 4b. Compared with the experimental results in Figure 3, we can assign all the peaks within the range of $\sim 0.3 - 0.7$ nm in Figure 4b to the 1st EDL layer. Within this layer, the principal cation and anion peaks are very close to each other (~ 0.8 Å separation) at PZC, with the cations being closer to the HOPG surface than the anions. This is likely due to the stronger vdW interaction between HOPG and the EMIM^+ compared to that of HOPG and TFSI^- , since the EMIM^+ cation contains a carbon-rich imidazolium ring and alkyl groups. At an electrode charge density of 0.28 e/nm^2 , the anions move closer to the HOPG, the density of their first peak increases, and the peak position is almost overlapping with the first cation peak; at a higher charge density of 0.55 e/nm^2 , the anions dominate the first peak while cations are pushed away, to a position ~ 2 Å above the anion. At negative electrode charges, the reverse trend occurs, with the anions being repelled away and the cations aggregating near the HOPG surface. This overall trend is consistent with our experimental observation that at higher potentials, either positive or negative, the 1st layer becomes wider, and confirms that such a widening is due to the separation of cations and anions driven by the interfacial electric field. At high enough potentials/electrode charges, *e.g.* -0.28 e/nm^2 and $\pm 0.55 \text{ e/nm}^2$, the cation and anion peaks become almost completely separated, which is in agreement with the experimental results at ± 1 V where the 1st layer splits into two layers.

To reveal the effect of the 1st layer on the EDL charge storage, we integrate the charge over this area and analyze their potential-dependence. As the electrode charge density changes from 0 to 0.28 e/nm^2 and 0.55 e/nm^2 , we find that the charge density of the first EDL (0–0.7 nm) changes

by -0.25 e/nm^2 and -0.57 e/nm^2 , respectively. At the reverse polarity, an electrode charge density shift from 0 to -0.28 e/nm^2 and -0.55 e/nm^2 results in an increase of charge density in the first EDL of 0.31 e/nm^2 and 0.56 e/nm^2 , respectively. These results reveal that, although the EDL consists of multiple discrete layers, the first layer nearly balances all the electrode charge and thus plays a dominant role in charge storage. This is consistent with our experimental results which reveal that the potential-dependent structural reconfiguration occurs mostly in the 1st EDL (Figure 3a).

We further quantify the molecular tilt effect by extracting the angular distribution of both the cations and the anions in the first layer. The results at different potentials are shown in Figure 4c. We can see that at high negative electrode charge, -0.55 e/nm^2 , the imidazolium ring of the cations is mostly parallel to the HOPG surface; as the potential increases, more cations become tilted, some becoming vertical and some oblique with an increasing tilt angle at more positive potential; at 0.55 e/nm^2 , most cations are either nearly vertical or have a tilt angle around $40^\circ/140^\circ$. The anions follow similar trend at reverse potential, with mostly parallel orientation at very positive potentials and tilted angles at negative potentials. These results agree well with the experimental x-z maps, and confirm our explanations: 1) high electrode potential attracts counter-ions to the surface and force them to become flat due to steric hindrance; and 2) at lower or reverse potential, these ions become more tilted due to thermal fluctuation and other intra-molecular/molecule-electrode interactions.

The above conclusions on the potential-dependent EDL reconfigurations can be visualized in the molecular snapshots from MD simulation. Since the molecules in EDL are dynamically moving and rotating during the MD simulation, snapshots of the structure of the 1st layer consist of molecules with a large variety of configurations. Representative molecular configurations are

shown in Figure 5. We observe the same potential-dependent position switching and tilting as explained above. Compared with the experimental x-z maps in Figure 3a, we can see that the quasi-periodic zigzag-like patterns are due to both the molecular tilt and the position offsets of the cations and anions. In addition, the MD snapshots reveal that the TFSI⁻ anions have two configurations, trans and cis. At the PZC, both trans and cis conformation exist. When the electrode is either positively or negatively charged, the trans conformation becomes more favorable in the first EDL, since the TFSI⁻ anions either adopt a flatter geometry due to attraction to the electrode, or become more vertical as they are repelled from the electrode surface.

CONCLUSION

In summary, we have developed an EC-3D-AFM technique, and used it to obtain molecular scale 3D maps of the EDL of ionic liquids at different electrode potentials. On an atomically clean HOPG surface, we observe discrete layers of EDL with quasi-periodic, zigzag-like oscillations. The width and oscillation features of the first EDL layer show pronounced reconfigurations upon the change of electrode potential, while other layers exhibit much weaker changes. Combining experimental results with MD simulation, we conclude that both the spatial arrangement and tilt angles of cations and anions in the first EDL are strongly dependent on electrode potential, and are key for capacitive charge storage. These mechanistic understandings can serve as guiding principles for the rational design of electrochemical energy storage systems such as supercapacitors and batteries.

METHODS

Sample and Tip Preparation. HOPG (ZYB grade, 12 mm × 12 mm × 2 mm) was purchased from Bruker. EMIM-TFSI (>98%) was purchased from Thermo Fischer Scientific. AFM probes

(FS-1500AuD) were purchased from Asylum Research, which have typical spring constants of 5–15 nN/nm. The tip material is Si/SiO₂ which is electrically insulating. After assembling the EC cell, HOPG was mechanically cleaved to expose a clean surface, right before EMIM-TFSI was added to the cell as electrolyte. The AFM probe was cleaned by soaking and rinsing with acetone, isopropanol, and DI water, followed by UV Ozone cleaning right before EC-3D-AFM measurements.

Electrochemical CV measurement. CV was performed using the AFM electrochemical cell in a nitrogen filled glovebox (H₂O and O₂ level are both <0.6 ppm). We used a CHI 600E electrochemical workstation. HOPG, Pt ring, and Pt wire serve as the working, reference, and counter electrodes, respectively. A circular area (9 mm diameter) of the HOPG surface was exposed to the electrolyte in the EC cell. The volume of the electrolyte used in CV and EC-3D-AFM measurements is typically in the range of 90 – 150 μ L. Photos of the liquid cup, the key part in the EC cell, are shown in Figure S9.

EC-3D-AFM Measurements. DC mode AFM measurements were performed using a Cypher ES AFM (Asylum Research, Oxford Instruments). Prior to each EC-3D-AFM experiment, we performed thermal tune of the AFM probe in air, in order to obtain the spring constant (k) value. After the EC cell was assembled and the AFM probe was fully immersed in the liquid electrolyte (an optical image of the immersed probe is shown in Figure S10), we first performed a quick large area scan (at least 100 \times 100 nm²) to confirm that the scanned area has atomic-scale smoothness. We then zoomed in to scan smaller areas. As the scanned area became 10 \times 10 nm² or smaller, we were typically able to observe lattice-resolution images of HOPG. Once lattice images were resolved, we switched to 3D-AFM mode to image the EDL structure. To apply an electrode potential, we used a Keithley sourcemeter, and manually changed the voltage in small

steps (e.g. 100 mV per step). After changing to each new voltage, we waited for at least five minutes to ensure the system reached equilibrium, before performing lateral imaging and 3D-AFM measurements. After 3D-AFM measurements at each non-zero voltage, we always switched back to 0 V to measure either the individual force curves or the 3D force map, to ensure that the 0 V results remained the same, as a proof that the tip remained unchanged.

2D lattice resolution images of HOPG surface were obtained using a scan rate of 4.88 Hz along the x axis. Single point force curves (e.g. results in Figure 2b) were measured at a z rate of 0.1 – 1 Hz using triangular piezo motion (linear approach and retraction). 3D-AFM was performed using sinusoidal z motion at a rate of 10 – 100 Hz. Using DC mode 3D-AFM, we recorded cantilever deflection values as a function of the three-dimensional position that the probe scanned through. All the measurements were carried out at room temperature, in a sealed EC cell under argon atmosphere.

Data Analysis. EC-3D-AFM data were processed using MATLAB. Force *vs* z curves, 1D histograms and 2D count maps were obtained from the observables (x, y, scanner extension (*Ext*) and cantilever deflection (*Defl*) values) in the 3D-AFM data. The *Defl* value at each (x, y) position was calibrated using the average InvOLS (inverse optical lever sensitivity) value calculated based on all the *Defl* *vs* *Ext* curves in the corresponding x-z frame. InvOLS varies slightly with different AFM probes and laser spot positions. Typical values we obtained for the FS-1500AuD probe are 11 – 13 nm/V. After calibrating the *Defl* values, we obtained the force as $F = k \cdot Defl$ and z values as $z = Defl - Ext$ with a zero offset to the HOPG surface, thus obtaining the F-z curves. The 1D histograms shown in Figure 3b were generated as the overall point count of the z values across each x-z frame. For each 1D histogram, a double-exponential fit was applied to fit the local minima and generate a smooth background (orange curves in

Figure 3b). This background, normalized by the number of x points in each x-z frame, was subtracted in the 2D x-z point count maps to produce images with clearer color contrast (e.g. Figures 2a and 3a). The 2D y-z count maps were generated following a similar procedure where all the calibrations and data analyses were done in the corresponding y-z frames. Further details can be found in the Supporting Information, Section 3.

MD Simulations. The MD simulations were carried out using the GROMACS software⁶⁰ with time step of 1 fs. The force field parameters for EMIM and TFSI were adopted from the All-Atom Optimized Potential for Liquid Simulations (OPLS-AA) forcefield.^{61,62} Simulations were performed first on a bulk EMIM-TFSI system (with no electrode) to obtain the bulk molecular density, and then on a slab system consisting of graphite/EMIM-TFSI/graphite where the number of species was tuned so that the molecular density at the center of the slab match that of the bulk system. Both systems were initially equilibrated in the NVT ensemble by a simulated annealing procedure with the following sequential steps: annealing at T=533 K for 1 ns, quenching from 533 K to 298 K for 1 ns, and equilibrating at 298 K for 1 ns. For the bulk system, the final configuration was further equilibrated for 2 ns followed by a production run of 10 ns in the NPT ensemble at a pressure of 1 atm and temperature of 298 K. The temperature and pressure were kept constant using the Nosé-Hoover thermostat⁶³ and Parrinello-Rahman barostat⁶⁴ with time constants of 0.2 ps and 1 ps, respectively. For the graphite/EMIM-TFSI/graphite system, the final configuration was equilibrated for a 5 ns followed by a 40 ns production run in the NVT ensemble at 298 K. For both systems, trajectories of the atoms were collected every 0.5 ps to obtain the results.

The simulated bulk system consists of 3680 molecules (half of them are EMIM, while the other half are TFSI). Periodic boundary conditions were applied in all directions. For the short-range

interactions, the cutoff radius was set to 1.2 nm. Both energy and pressure tail corrections have been applied to the standard 12-6 LJ potential for the bulk MD simulations.⁶⁵ The long-range electrostatic interactions were calculated using the particle mesh Ewald (PME) summation⁶⁶ with a cutoff radius of 1.2 nm and fast Fourier transform (FFT) grid spacing of 0.12 nm. The bulk molecular density for each species was calculated using the final 6 ns trajectory of the NPT production simulation and is equal to 2.438 nm⁻³.

For the graphite/EMIM-TFSI/graphite slab system, the electrolyte is sandwiched between two graphite sheets separated by distance of 16 nm (between the inner surfaces of graphite) in the z direction. The lateral dimensions of the sheets are 7.122 × 7.232 nm². The long-range Coulombic interactions were treated using the Ewald3DC method adapted for the slab geometry.⁶⁷ The LJ length and energy scale parameters for carbon atoms are 0.340 nm and 0.23279 kJ/mol, respectively. Periodic boundary conditions were applied in all the directions with an extra vacuum of 35 nm in the z direction to avoid slab-slab interactions between periodic images. During the simulation, the graphite electrodes were frozen, *i.e.*, their positions were fixed. To simulate the effect of electrode voltages, we uniformly distributed charges in the inner graphene layer (in contact with the electrolyte). For each system, the equilibrium properties were averaged over a set of 3 MD simulations each with different initial velocities and positions.

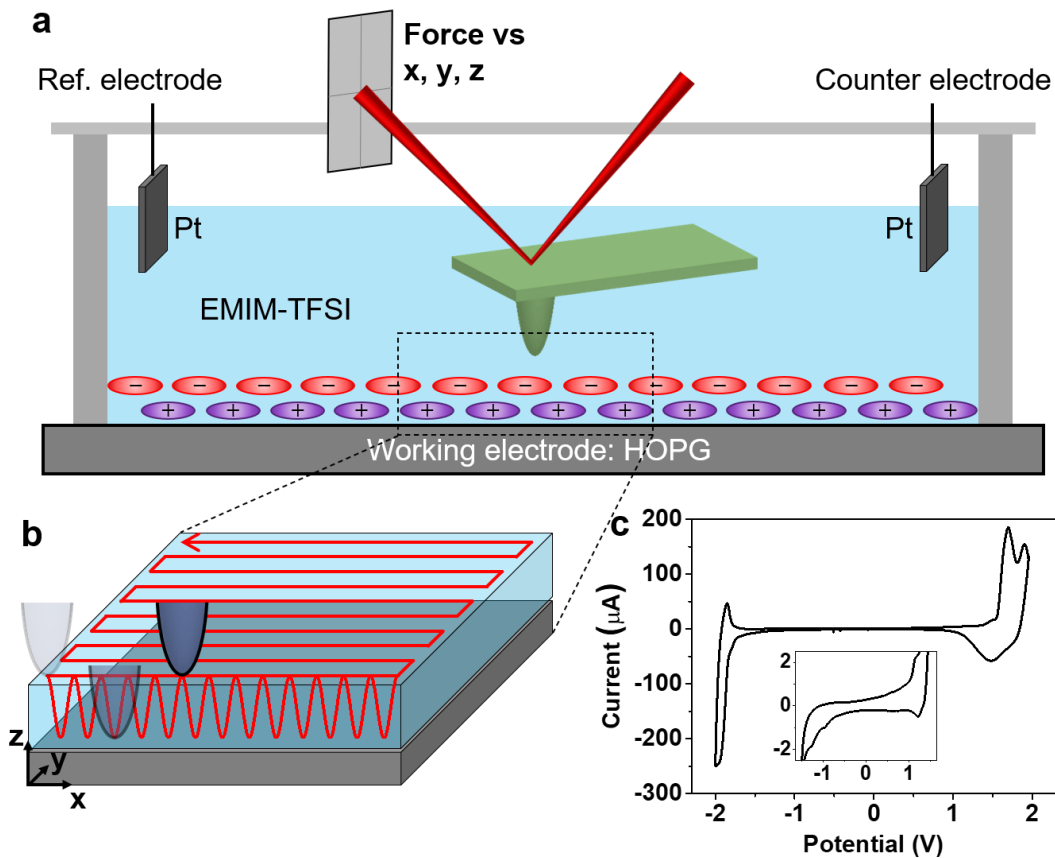


Figure 1. Measurement schematics and electrochemical tests. (a) Schematic diagram of the EC-3D-AFM setup. (b) Schematic of the high-speed 3D force mapping method. (c) CV of the EMIM-TFSI on HOPG in the EC cell as shown in (a). Inset is a CV sweep over a smaller potential range (-1.5 – 1.5 V vs Pt). CV sweep rate: 10 mV/s.

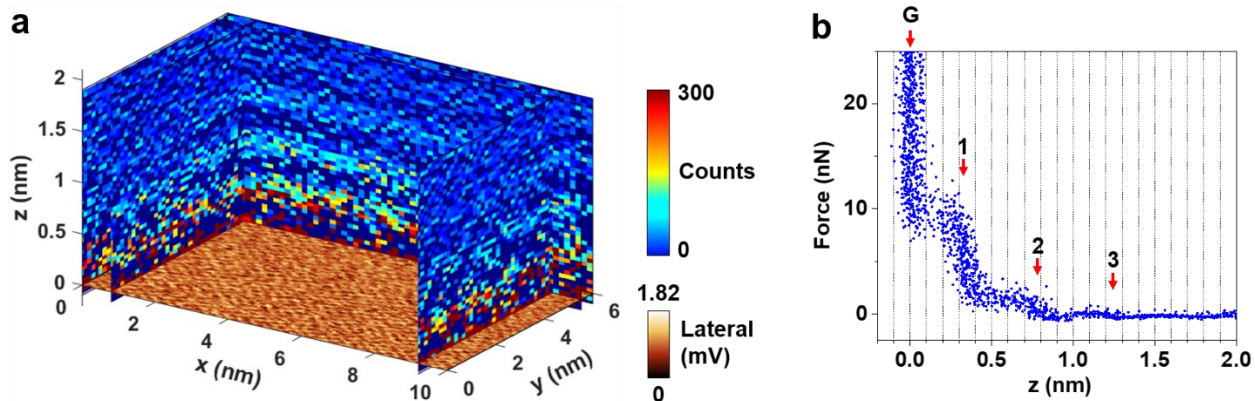


Figure 2. 3D-AFM results at 0 V (vs Pt). (a) 3D image of one area of the electrode-electrolyte interface, consisting of the x-y lateral image of HOPG surface and the x-z and y-z count maps revealing the EDL of EMIM-TFSI. (b) A series of 50 force-distance curves on top of a clean spot of HOPG. Red arrows mark the positions where the force increases sharply, corresponding to the HOPG surface (G) and the first three EDL layers.

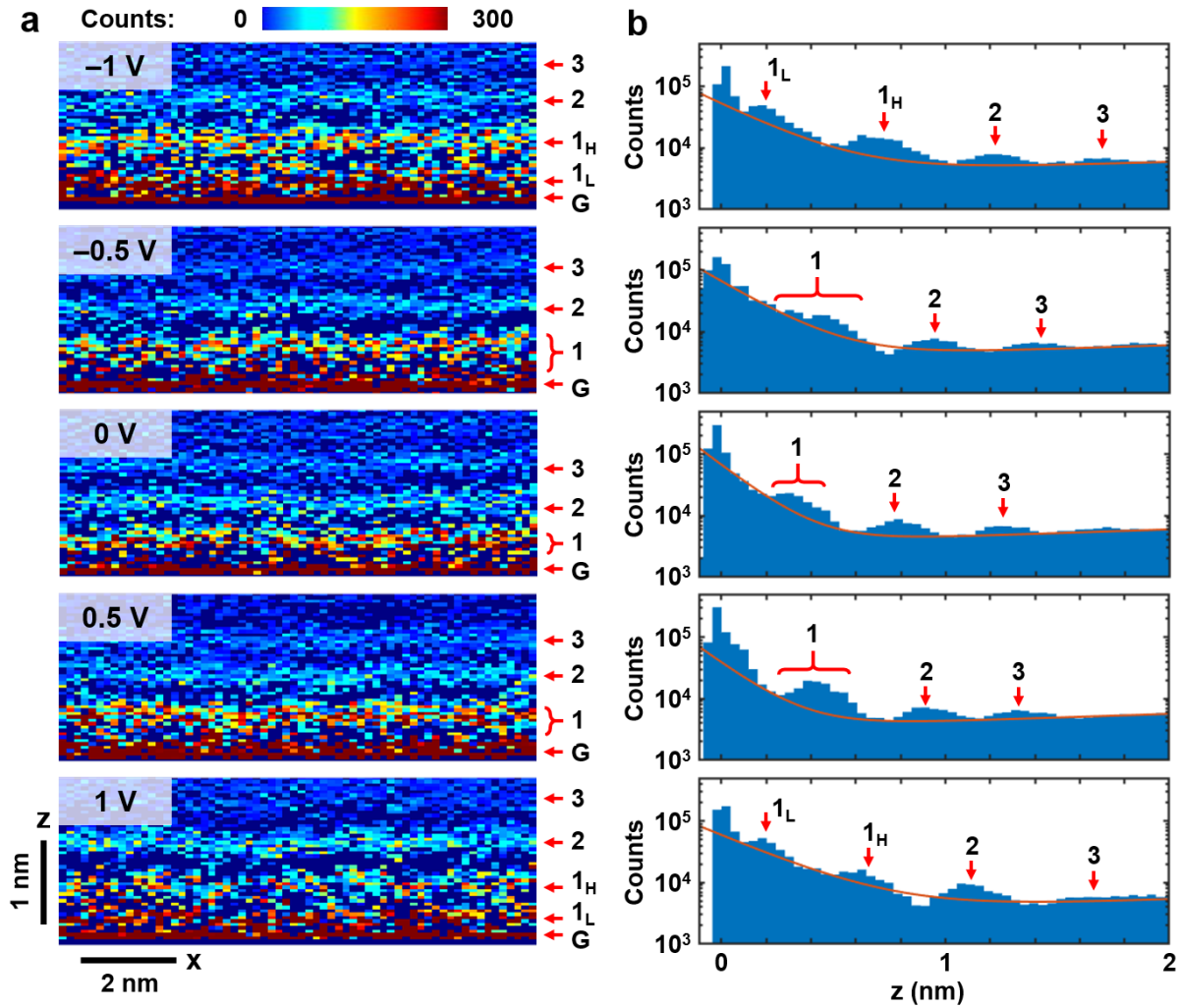


Figure 3. EC-3D-AFM results of the potential-dependent EDL structure. (a) x-z count maps at different electrode potential. (b) The corresponding point count histograms as a function of z , where the orange curves are the fits to the local minima of the histograms. Red arrows and curly brackets mark the positions of the HOPG surface and the first three EDL layers. 1_L and 1_H represent the lower and upper 1st layer, respectively.

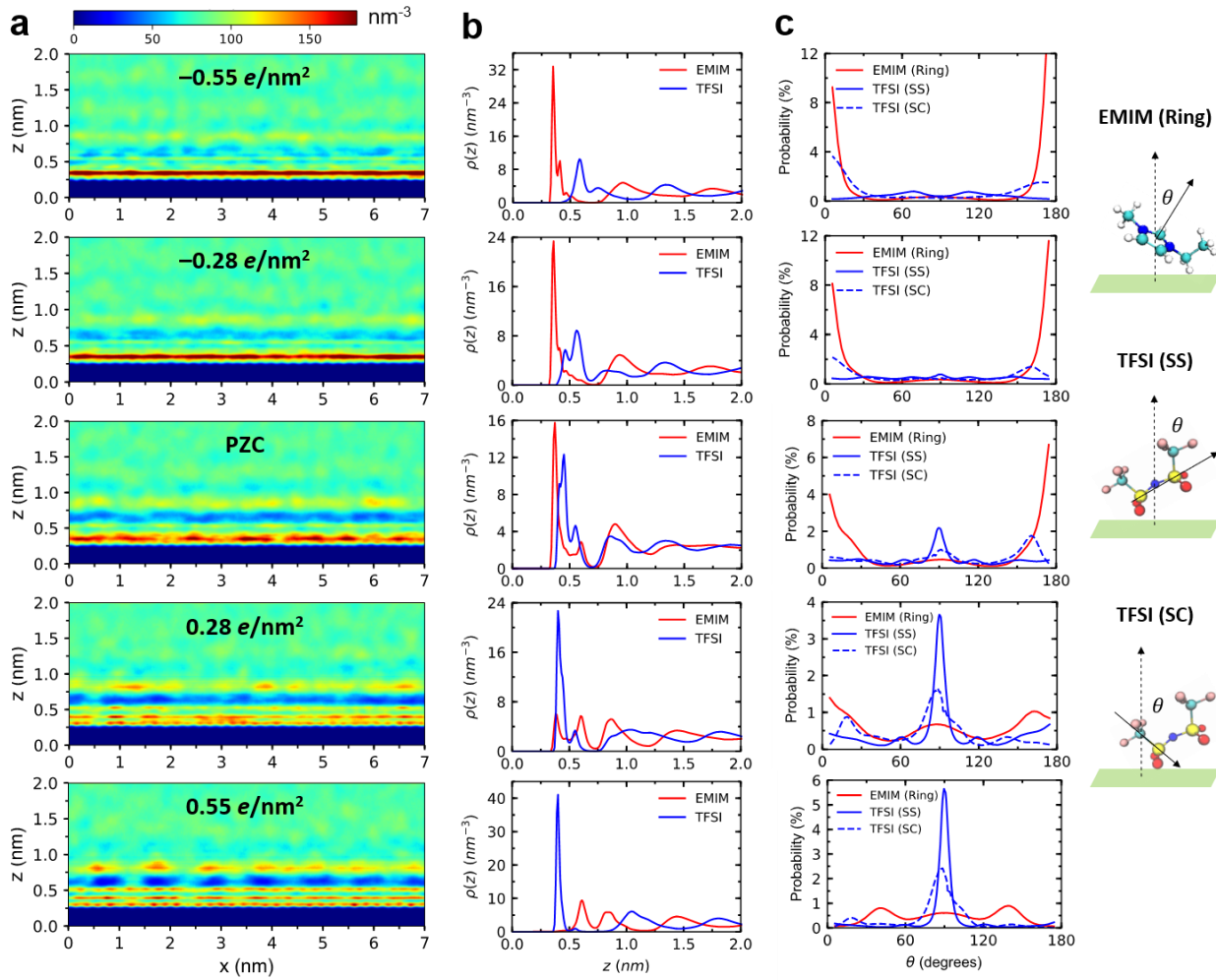


Figure 4. MD simulations of the x-z atomic density distribution maps (a), center-of-mass distribution of EMIM^+ cations and TFSI^- anions along the z direction (b), and the angular distribution of the molecules within the first EDL (in the z range of 0–0.7 nm) (c). The corresponding electrode charge densities of the simulated systems are marked in (a).

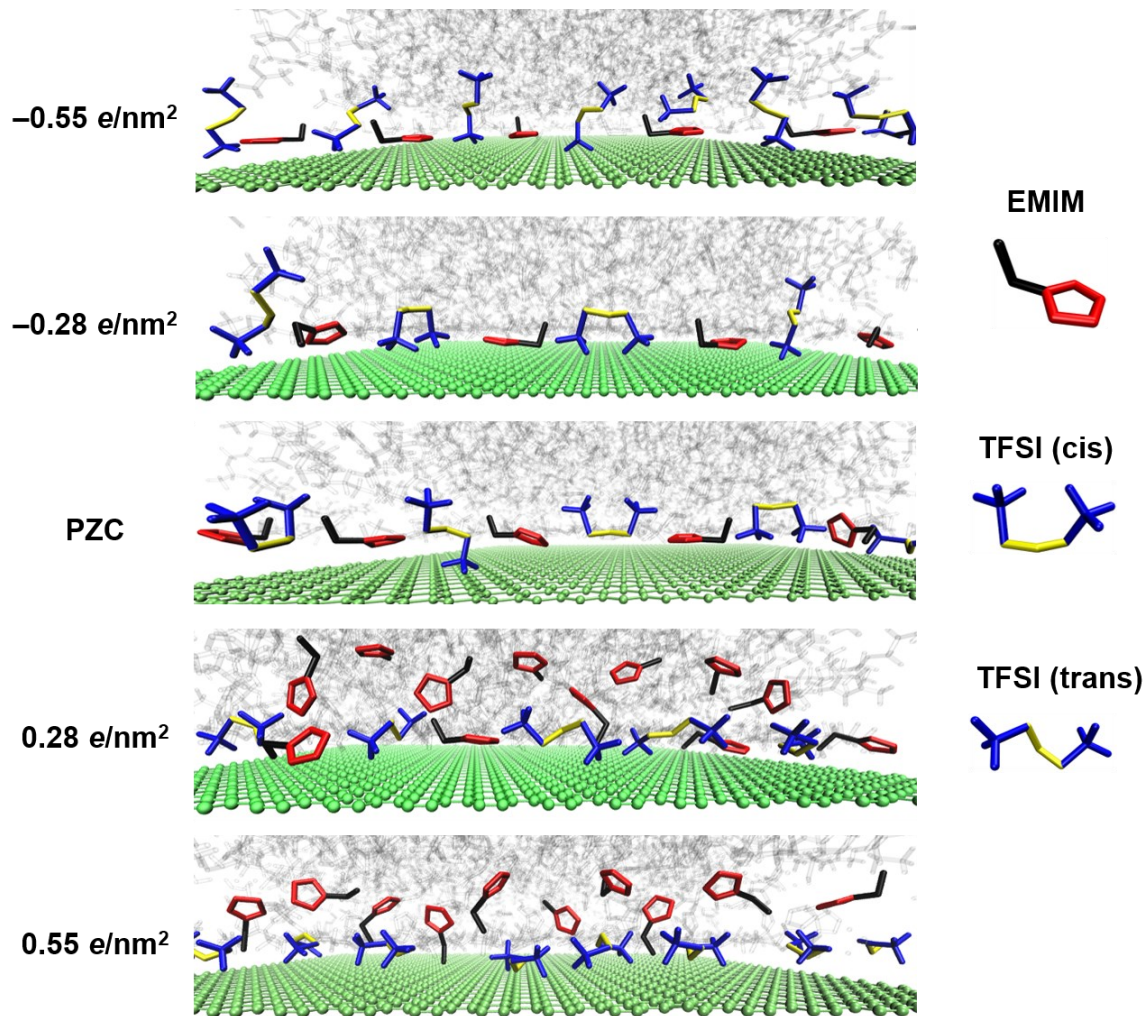


Figure 5. MD snapshots of the molecular configurations at the graphite – electrolyte interface at different electrode charge densities. For the electrode, only the top graphene sheet (out of the four layers) is shown. The EMIM^+ cations are represented by their imidazolium ring (red) and ethyl side chain (black), while the TFSI^- anions are depicted by the nitrogen-sulfur bond (yellow) and sulfur-carbon and carbon-fluorine bonds (blue).

ASSOCIATED CONTENT

Supporting Information. The following files are available free of charge at the ACS Publications website.

1. Pdf file containing: Cyclic voltammetry and charge density quantification; AFM images of HOPG surface; DC mode EC-3D-AFM data analysis procedures; AC mode EC-3D-AFM procedures and results; configuration of the molecular dynamics simulation; simulated charge and potential profiles; photos of the liquid cup of the electrochemical cell; optical image of the probe.
2. Movies showing 3D count maps extracted from DC mode EC-3D-AFM data, at five different electrode potentials: 0, ± 0.5 V and ± 1 V (vs Pt).

Notes

The authors declare no competing financial interest.

ACKNOWLEDGMENTS

Acknowledgment is made to the Donors of the American Chemical Society Petroleum Research Fund for support of this research (S.Z., K.S.P. and Y.Z.). The experiments were performed in part in the Carl R. Woese Institute for Genomic Biology and in the Materials Research Laboratory at the University of Illinois. S.Z., K.S.P. and Y.Z. acknowledge the use of facilities and instrumentation supported by the National Science Foundation (NSF) through the University of Illinois Materials Research Science and Engineering Center (DMR-1720633). M.H.M. and N.R.A. were supported by NSF under Grants 1545907, 1708852, 1720633, and 1921578. The computing power is provided by the Extreme Science and Engineering Discovery Environment (XSEDE) granted by NSF with Grant No. OCI-1053575 and Blue Waters supercomputing center, awarded by the state of Illinois and NSF, OCI-0725070, ACI-1238993.

REFERENCES

(1) Stamenkovic, V. R.; Strmcnik, D.; Lopes, P. P.; Markovic, N. M. Energy and Fuels from Electrochemical Interfaces. *Nat. Mater.* **2017**, *16*, 57–69.

(2) Fedorov, M. V.; Kornyshev, A. A. Ionic Liquids at Electrified Interfaces. *Chem. Rev.* **2014**, *114*, 2978–3036.

(3) Pham, T. A.; Ping, Y.; Galli, G. Modelling Heterogeneous Interfaces for Solar Water Splitting. *Nat. Mater.* **2017**, *16*, 401–408.

(4) Xu, K. Electrolytes and Interphases in Li-Ion Batteries and Beyond. *Chem. Rev.* **2014**, *114*, 11503–11618.

(5) Shannon, M. A.; Bohn, P. W.; Elimelech, M.; Georgiadis, J. G.; Mariñas, B. J.; Mayes, A. M. Science and Technology for Water Purification in the Coming Decades. *Nature* **2008**, *452*, 301–310.

(6) Liu, C.; Kong, D.; Hsu, P.-C.; Yuan, H.; Lee, H.-W.; Liu, Y.; Wang, H.; Wang, S.; Yan, K.; Lin, D.; Maraccini, P. A.; Parker, K. M.; Boehm, A. B.; Cui, Y. Rapid Water Disinfection Using Vertically Aligned MoS₂ Nanofilms and Visible Light. *Nat. Nanotechnol.* **2016**, *11*, 1098–1104.

(7) Maurice, V.; Marcus, P. Progress in Corrosion Science at Atomic and Nanometric Scales. *Prog. Mater. Sci.* **2018**, *95*, 132–171.

(8) Ball, P. Water as an Active Constituent in Cell Biology. *Chem. Rev.* **2008**, *108*, 74–108.

(9) Laage, D.; Elsaesser, T.; Hynes, J. T. Water Dynamics in the Hydration Shells of Biomolecules. *Chem. Rev.* **2017**, *117*, 10694–10725.

(10) Israelachvili, J.; Wennerström, H. Role of Hydration and Water Structure in Biological and Colloidal Interactions. *Nature* **1996**, *379*, 219–225.

(11) Griffin, J. M.; Forse, A. C.; Tsai, W.-Y.; Taberna, P.-L.; Simon, P.; Grey, C. P. *In Situ* NMR and Electrochemical Quartz Crystal Microbalance Techniques Reveal the Structure of the Electrical Double Layer in Supercapacitors. *Nat. Mater.* **2015**, *14*, 812–819.

(12) Simon, P.; Gogotsi, Y. Perspectives for Electrochemical Capacitors and Related Devices. *Nat. Mater.* **2020**, *19*, 1151–1163.

(13) Liu, T.; Lin, L.; Bi, X.; Tian, L.; Yang, K.; Liu, J.; Li, M.; Chen, Z.; Lu, J.; Amine, K.; Xu, K.; Pan, F. *In Situ* Quantification of Interphasial Chemistry in Li-Ion Battery. *Nat. Nanotechnol.* **2019**, *14*, 50–56.

(14) Zhou, Y.; Su, M.; Yu, X.; Zhang, Y.; Wang, J.-G.; Ren, X.; Cao, R.; Xu, W.; Baer, D. R.; Du, Y.; Borodin, O.; Wang, Y.; Wang, X.-L.; Xu, K.; Xu, Z.; Wang, C.; Zhu, Z. Real-Time Mass Spectrometric Characterization of the Solid–Electrolyte Interphase of a Lithium-Ion Battery. *Nat. Nanotechnol.* **2020**, *15*, 224–230.

(15) Xu, K. “Charge-Transfer” Process at Graphite/Electrolyte Interface and the Solvation Sheath Structure of Li⁺ in Nonaqueous Electrolytes. *J. Electrochem. Soc.* **2007**, *154*, A162.

(16) Su, C.-C.; He, M.; Amine, R.; Rojas, T.; Cheng, L.; Ngo, A. T.; Amine, K. Solvating Power Series of Electrolyte Solvents for Lithium Batteries. *Energy Environ. Sci.* **2019**, *12*, 1249–1254.

(17) von Wald Cresce, A.; Borodin, O.; Xu, K. Correlating Li^+ Solvation Sheath Structure with Interphasial Chemistry on Graphite. *J. Phys. Chem. C* **2012**, *116*, 26111–26117.

(18) Rakov, D. A.; Chen, F.; Ferdousi, S. A.; Li, H.; Pathirana, T.; Simonov, A. N.; Howlett, P. C.; Atkin, R.; Forsyth, M. Engineering High-Energy-Density Sodium Battery Anodes for Improved Cycling with Superconcentrated Ionic-Liquid Electrolytes. *Nat. Mater.* **2020**, *19*, 1096–1101.

(19) Wang, H.; Wu, C. H.; Eren, B.; Hao, Y.; Feng, B.; Fang, H.-T.; Salmeron, M. Operando STM Study of the Interaction of Imidazolium-Based Ionic Liquid with Graphite. *Energy Storage Mater.* **2019**, *20*, 139–145.

(20) Velasco-Velez, J.-J.; Wu, C. H.; Pascal, T. A.; Wan, L. F.; Guo, J.; Prendergast, D.; Salmeron, M. The Structure of Interfacial Water on Gold Electrodes Studied by X-Ray Absorption Spectroscopy. *Science* **2014**, *346*, 831–834.

(21) Li, C.-Y.; Le, J.-B.; Wang, Y.-H.; Chen, S.; Yang, Z.-L.; Li, J.-F.; Cheng, J.; Tian, Z.-Q. *In Situ* Probing Electrified Interfacial Water Structures at Atomically Flat Surfaces. *Nat. Mater.* **2019**, *18*, 697–701.

(22) Mao, X.; Brown, P.; Červinka, C.; Hazell, G.; Li, H.; Ren, Y.; Chen, D.; Atkin, R.; Eastoe, J.; Grillo, I.; Padua, A. A. H.; Gomes, M. F. C.; Hatton, T. A. Self-Assembled Nanostructures in Ionic Liquids Facilitate Charge Storage at Electrified Interfaces. *Nat. Mater.* **2019**, *18*, 1350–1357.

(23) Zhang, X.; Zhong, Y.-X.; Yan, J.-W.; Su, Y.-Z.; Zhang, M.; Mao, B.-W. Probing Double Layer Structures of Au (111)–BMIPF₆ Ionic Liquid Interfaces from Potential-Dependent AFM Force Curves. *Chem. Commun.* **2012**, *48*, 582–584.

(24) Black, J. M.; Walters, D.; Labuda, A.; Feng, G.; Hillesheim, P. C.; Dai, S.; Cummings, P. T.; Kalinin, S. V; Proksch, R.; Balke, N. Bias-Dependent Molecular-Level Structure of Electrical Double Layer in Ionic Liquid on Graphite. *Nano Lett.* **2013**, *13*, 5954–5960.

(25) Hayes, R.; Borisenko, N.; Tam, M. K.; Howlett, P. C.; Endres, F.; Atkin, R. Double Layer Structure of Ionic Liquids at the Au(111) Electrode Interface: An Atomic Force Microscopy Investigation. *J. Phys. Chem. C* **2011**, *115*, 6855–6863.

(26) Segura, J. J.; Elbourne, A.; Wanless, E. J.; Warr, G. G.; Voïtchovsky, K.; Atkin, R. Adsorbed and Near Surface Structure of Ionic Liquids at a Solid Interface. *Phys. Chem. Chem. Phys.* **2013**, *15*, 3320–3328.

(27) Jurado, L. A.; Espinosa-Marzal, R. M. Insight into the Electrical Double Layer of an Ionic Liquid on Graphene. *Sci. Rep.* **2017**, *7*, 4225.

(28) Sheehan, A.; Jurado, L. A.; Ramakrishna, S. N.; Arcifa, A.; Rossi, A.; Spencer, N. D.; Espinosa-Marzal, R. M. Layering of Ionic Liquids on Rough Surfaces. *Nanoscale* **2016**, *8*, 4094–4106.

(29) Hayes, R.; El Abedin, S. Z.; Atkin, R. Pronounced Structure in Confined Aprotic Room-Temperature Ionic Liquids. *J. Phys. Chem. B* **2009**, *113*, 7049–7052.

(30) Black, J. M.; Zhu, M.; Zhang, P.; Unocic, R. R.; Guo, D.; Okatan, M. B.; Dai, S.; Cummings, P. T.; Kalinin, S. V.; Feng, G.; Balke, N. Fundamental Aspects of Electric Double Layer Force-Distance Measurements at Liquid-Solid Interfaces Using Atomic Force Microscopy. *Sci. Rep.* **2016**, *6*, 32389.

(31) Cui, T.; Lahiri, A.; Carstens, T.; Borisenco, N.; Pulletikurthi, G.; Kuhl, C.; Endres, F. Influence of Water on the Electrified Ionic Liquid/Solid Interface: A Direct Observation of the Transition from a Multilayered Structure to a Double-Layer Structure. *J. Phys. Chem. C* **2016**, *120*, 9341–9349.

(32) Umeda, K.; Zivanovic, L.; Kobayashi, K.; Ritala, J.; Kominami, H.; Spijker, P.; Foster, A. S.; Yamada, H. Atomic-Resolution Three-Dimensional Hydration Structures on a Heterogeneously Charged Surface. *Nat. Commun.* **2017**, *8*, 2111.

(33) Umeda, K.; Kobayashi, K.; Minato, T.; Yamada, H. Atomic-Scale 3D Local Hydration Structures Influenced by Water-Restricting Dimensions. *Langmuir* **2018**, *34*, 9114–9121.

(34) Umeda, K.; Kobayashi, K.; Minato, T.; Yamada, H. Atomic-Level Viscosity Distribution in the Hydration Layer. *Phys. Rev. Lett.* **2019**, *122*, 116001.

(35) Martin-Jimenez, D.; Chacon, E.; Tarazona, P.; Garcia, R. Atomically Resolved Three-Dimensional Structures of Electrolyte Aqueous Solutions Near a Solid Surface. *Nat. Commun.* **2016**, *7*, 12164.

(36) Martin-Jimenez, D.; Garcia, R. Identification of Single Adsorbed Cations on Mica–Liquid Interfaces by 3D Force Microscopy. *J. Phys. Chem. Lett.* **2017**, *8*, 5707–5711.

(37) Uhlig, M. R.; Martin-Jimenez, D.; Garcia, R. Atomic-Scale Mapping of Hydrophobic Layers on Graphene and Few-Layer MoS₂ and WSe₂ in Water. *Nat. Commun.* **2019**, *10*, 2606.

(38) Söngen, H.; Reischl, B.; Miyata, K.; Bechstein, R.; Raiteri, P.; Rohl, A. L.; Gale, J. D.; Fukuma, T.; Kühnle, A. Resolving Point Defects in the Hydration Structure of Calcite (10.4) with Three-Dimensional Atomic Force Microscopy. *Phys. Rev. Lett.* **2018**, *120*, 116101.

(39) Miyazawa, K.; Watkins, M.; Shluger, A. L.; Fukuma, T. Influence of Ions on Two-Dimensional and Three-Dimensional Atomic Force Microscopy at Fluorite–Water Interfaces. *Nanotechnology* **2017**, *28*, 245701.

(40) Labuda, A.; Grütter, P. Atomic Force Microscopy in Viscous Ionic Liquids. *Langmuir* **2012**, *28*, 5319–5322.

(41) Ichii, T.; Negami, M.; Sugimura, H. Atomic-Resolution Imaging on Alkali Halide Surfaces in Viscous Ionic Liquid Using Frequency Modulation Atomic Force Microscopy. *J. Phys. Chem. C* **2014**, *118*, 26803–26807.

(42) Harada, T.; Yokota, Y.; Imanishi, A.; Fukui, K. Preferential Formation of Layered Structure of Ionic Liquid at Ionic Liquid Aqueous Solution / Graphite Electrode Interfaces Observed by Frequency-Modulation Atomic Force Microscopy. *E.-J. Surf. Sci. Nanotechnol.* **2014**, *12*, 89–96.

(43) Panse, K. S.; Zhou, S.; Zhang, Y. 3D Mapping of the Structural Transitions in Wrinkled 2D Membranes: Implications for Reconfigurable Electronics, Memristors, and Bioelectronic Interfaces. *ACS Appl. Nano Mater.* **2019**, *2*, 5779–5786.

(44) Richey, F. W.; Dyatkin, B.; Gogotsi, Y.; Elabd, Y. A. Ion Dynamics in Porous Carbon Electrodes in Supercapacitors Using *In Situ* Infrared Spectroelectrochemistry. *J. Am. Chem. Soc.* **2013**, *135*, 12818–12826.

(45) Hyun, W. J.; de Moraes, A. C. M.; Lim, J.-M.; Downing, J. R.; Park, K.-Y.; Tan, M. T. Z.; Hersam, M. C. High-Modulus Hexagonal Boron Nitride Nanoplatelet Gel Electrolytes for Solid-State Rechargeable Lithium-Ion Batteries. *ACS Nano* **2019**, *13*, 9664–9672.

(46) Guerfi, A.; Dontigny, M.; Charest, P.; Petitclerc, M.; Lagacé, M.; Vijh, A.; Zaghib, K. Improved Electrolytes for Li-Ion Batteries: Mixtures of Ionic Liquid and Organic Electrolyte with Enhanced Safety and Electrochemical Performance. *J. Power Sources* **2010**, *195*, 845–852.

(47) Umeda, K.; Kobayashi, K.; Minato, T.; Yamada, H. Atomic-Scale Three-Dimensional Local Solvation Structures of Ionic Liquids. *J. Phys. Chem. Lett.* **2020**, *11*, 1343–1348.

(48) Fukuma, T.; Ueda, Y.; Yoshioka, S.; Asakawa, H. Atomic-Scale Distribution of Water Molecules at the Mica-Water Interface Visualized by Three-Dimensional Scanning Force Microscopy. *Phys. Rev. Lett.* **2010**, *104*, 16101.

(49) Yamagata, M.; Nishigaki, N.; Nishishita, S.; Matsui, Y.; Sugimoto, T.; Kikuta, M.; Higashizaki, T.; Kono, M.; Ishikawa, M. Charge–Discharge Behavior of Graphite Negative Electrodes in Bis(Fluorosulfonyl)Imide-Based Ionic Liquid and Structural Aspects of Their Electrode/Electrolyte Interfaces. *Electrochim. Acta* **2013**, *110*, 181–190.

(50) Fan, J.; Xiao, Q.; Fang, Y.; Li, L.; Feng, W.; Yuan, W. Reversible Intercalation of 1-Ethyl-3-Methylimidazolium Cations into MoS₂ from a Pure Ionic Liquid Electrolyte for Dual-Ion Cells. *ChemElectroChem* **2019**, *6*, 676–683.

(51) Xue, Z.; Qin, L.; Jiang, J.; Mu, T.; Gao, G. Thermal, Electrochemical and Radiolytic Stabilities of Ionic Liquids. *Phys. Chem. Chem. Phys.* **2018**, *20*, 8382–8402.

(52) Klein, J. M.; Panichi, E.; Gurkan, B. Potential Dependent Capacitance of [EMIM][TFSI], [N₁₁₁₄][TFSI] and [PYR₁₃][TFSI] Ionic Liquids on Glassy Carbon. *Phys. Chem. Chem. Phys.* **2019**, *21*, 3712–3720.

(53) Hayyan, M.; Mjalli, F. S.; Hashim, M. A.; AlNashef, I. M.; Mei, T. X. Investigating the Electrochemical Windows of Ionic Liquids. *J. Ind. Eng. Chem.* **2013**, *19*, 106–112.

(54) Gan, Y.; Franks, G. V. High Resolution AFM Images of the Single-Crystal α -Al₂O₃(0001) Surface in Water. *J. Phys. Chem. B* **2005**, *109*, 12474–12479.

(55) Sharp, T. G.; Oden, P. I.; Buseck, P. R. Lattice-Scale Imaging of Mica and Clay (001) Surfaces by Atomic Force Microscopy Using Net Attractive Forces. *Surf. Sci. Lett.* **1993**, *284*, L405–L410.

(56) Rode, S.; Oyabu, N.; Kobayashi, K.; Yamada, H.; Kühnle, A. True Atomic-Resolution Imaging of (10 $\overline{1}$ 4) Calcite in Aqueous Solution by Frequency Modulation Atomic Force Microscopy. *Langmuir* **2009**, *25*, 2850–2853.

(57) Largeot, C.; Portet, C.; Chmiola, J.; Taberna, P.-L.; Gogotsi, Y.; Simon, P. Relation between the Ion Size and Pore Size for an Electric Double-Layer Capacitor. *J. Am. Chem. Soc.* **2008**, *130*, 2730–2731.

(58) Elbourne, A.; McDonald, S.; Voïchovsky, K.; Endres, F.; Warr, G. G.; Atkin, R. Nanostructure of the Ionic Liquid–Graphite Stern Layer. *ACS Nano* **2015**, *9*, 7608–7620.

(59) Haskins, J. B.; Lawson, J. W. Evaluation of Molecular Dynamics Simulation Methods for Ionic Liquid Electric Double Layers. *J. Chem. Phys.* **2016**, *144*, 184707.

(60) Abraham, M. J.; Murtola, T.; Schulz, R.; Páll, S.; Smith, J. C.; Hess, B.; Lindahl, E. GROMACS: High Performance Molecular Simulations through Multi-Level Parallelism from Laptops to Supercomputers. *SoftwareX* **2015**, *1–2*, 19–25.

(61) Sambasivarao, S. V.; Acevedo, O. Development of OPLS-AA Force Field Parameters for 68 Unique Ionic Liquids. *J. Chem. Theory Comput.* **2009**, *5*, 1038–1050.

(62) Doherty, B.; Zhong, X.; Gathiaka, S.; Li, B.; Acevedo, O. Revisiting OPLS Force Field Parameters for Ionic Liquid Simulations. *J. Chem. Theory Comput.* **2017**, *13*, 6131–6145.

(63) Nosé, S. A Unified Formulation of the Constant Temperature Molecular Dynamics Methods. *J. Chem. Phys.* **1984**, *81*, 511–519.

(64) Parrinello, M.; Rahman, A. Polymorphic Transitions in Single Crystals: A New Molecular Dynamics Method. *J. Appl. Phys.* **1981**, *52*, 7182–7190.

(65) Chialvo, A. A.; Cummings, P. T. Molecular-Based Modeling of Water and Aqueous Solutions at Supercritical Conditions. Advances in Chemical Physics. *Adv. Chem. Phys.* **1999**, *109*, 115–205.

(66) Darden, T.; York, D.; Pedersen, L. Particle Mesh Ewald: An N·log(N) Method for Ewald Sums in Large Systems. *J. Chem. Phys.* **1993**, *98*, 10089–10092.

(67) Yeh, I.-C.; Berkowitz, M. L. Ewald Summation for Systems with Slab Geometry. *J. Chem. Phys.* **1999**, *111*, 3155–3162.